Electric-field-driven electron-transfer in mixed-valence molecules

Enrique P. Blair,[1,a)] Steven A. Corcelli,[2,b)] and Craig S. Lent[3,c)]
[1]*Department of Electrical and Computer Engineering, Baylor University, Waco, Texas 76798, USA*
[2]*Department of Chemistry and Biochemistry, University of Notre Dame, Notre Dame, Indiana 46556, USA*
[3]*Department of Electrical Engineering, University of Notre Dame, Notre Dame, Indiana 46556, USA*

(Received 29 March 2016; accepted 21 June 2016; published online 6 July 2016)

Molecular quantum-dot cellular automata is a computing paradigm in which digital information is encoded by the charge configuration of a mixed-valence molecule. General-purpose computing can be achieved by arranging these compounds on a substrate and exploiting intermolecular Coulombic coupling. The operation of such a device relies on nonequilibrium electron transfer (ET), whereby the time-varying electric field of one molecule induces an ET event in a neighboring molecule. The magnitude of the electric fields can be quite large because of close spatial proximity, and the induced ET rate is a measure of the nonequilibrium response of the molecule. We calculate the electric-field-driven ET rate for a model mixed-valence compound. The mixed-valence molecule is regarded as a two-state electronic system coupled to a molecular vibrational mode, which is, in turn, coupled to a thermal environment. Both the electronic and vibrational degrees-of-freedom are treated quantum mechanically, and the dissipative vibrational-bath interaction is modeled with the Lindblad equation. This approach captures both tunneling and nonadiabatic dynamics. Relationships between microscopic molecular properties and the driven ET rate are explored for two time-dependent applied fields: an abruptly switched field and a linearly ramped field. In both cases, the driven ET rate is only weakly temperature dependent. When the model is applied using parameters appropriate to a specific mixed-valence molecule, diferrocenylacetylene, terahertz-range ET transfer rates are predicted. *Published by AIP Publishing.* [http://dx.doi.org/10.1063/1.4955113]

I. INTRODUCTION

Mixed-valence molecules have been proposed for use in molecular-based quantum-dot cellular automata (QCA).[1–9] In molecular QCA, digital information is encoded by the charge distribution of a molecule. Symmetric, mixed-valence molecules containing two metal centers are ideal for such an application because they are intrinsically digital. When an electron is localized on the left metal site, and the molecule represents a "0" bit. After an electron transfer (ET) event, the electron is localized on the right metal center, the molecule then represents a "1" bit. General purpose QCA computing is achieved by arranging the mixed-valence molecules on a substrate, where neighboring molecules are coupled by their Coulombic interaction.[10–13] The operation of such a device involves nonequilibrium ET events in individual molecules that are driven by the time-varying electric fields of neighboring molecules. An important challenge is to understand the electric-field-driven ET process to design mixed-valence molecules with optimal properties for molecular QCA applications.

ET is a key mechanism underlying numerous processes studied in the biological, chemical, and physical sciences.[14–16] Marcus' seminal contribution to the theory of ET in condensed-phase matter built on transition-state theory to first model ET between molecules in a solvent.[17] Later, this theory was extended by Hush to describe intramolecular ET.[18] This theory is semiclassical, treating the electron quantum mechanically and nuclear vibrations associated with the intramolecular ET classically. Others, like Jortner, have provided fully quantum treatments of the nuclear vibrational modes and rely on perturbation theory to calculate the ET rate.[19,20] This ET process is enabled by thermal fluctuations in the solvent field, which averages over time to a net-zero field, and the rate calculated is an equilibrium property.

Here, the objective is to model nonequilibrium ET in mixed-valence molecules that are subjected to time-varying external electric fields. In the context of QCA, the external field originates from Coulombic interactions with neighboring molecules. In such a design, it is essential that the mixed-valence molecules utilize suitable linkers which promote intramolecular ET over intermolecular ET. The differences between conventional equilibrium thermally driven ET processes and the nonequilibrium field-driven ET processes of interest in the present work are seen in a comparison of Figures 1 and 2.

In thermally driven ET (Figure 1), the adiabatic potential energy for the system (blue curve) is constant in time. The reaction coordinate, Q, is a collective solvent polarization in outer-sphere ET and is an intramolecular vibrational mode in inner-sphere ET. In either case, the reaction coordinate is in thermal equilibrium and the population of stable states, P_A and P_B, is static. Forward ($A \rightarrow B$) and reverse ($B \rightarrow A$) ET reactions are driven by fluctuations and are characterized by rate constants $k_{A\rightarrow B}$ and $k_{B\rightarrow A}$. The rate constants are equilibrium properties that obey the usual detailed balance criterion $k_{A\rightarrow B}/k_{B\rightarrow A} = P_B/P_A$.

a)enrique_blair@baylor.edu
b)scorcell@nd.edu
c)lent@nd.edu

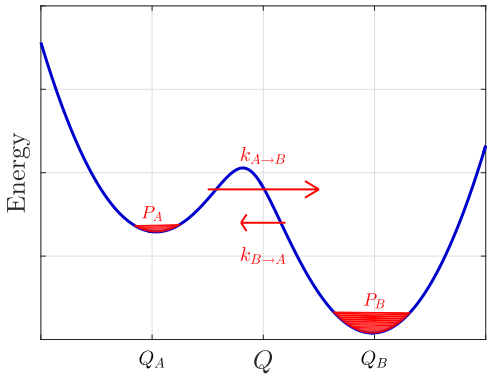

FIG. 1. A thermally driven equilibrium ET process. A constant adiabatic potential energy surface V (blue line) as a function of reaction coordinate Q has a barrier between two potential wells. Here, two populations (red areas) are in thermal equilibrium.

In contrast to these processes, ET in mixed-valence molecules can also be induced by a time-varying electric field (Figures 2(a) and 2(b)). In this case, the system of interest is a molecule with two charge-localization centers. Initially, the electronic and nuclear degrees-of-freedom of the mixed-valence molecule are in equilibrium at $t = 0$ with a thermal environment. This is the situation shown in the left panel of Figure 2(a). The electron is localized on the left metal center and the vibrational states of the molecule have populations that are Boltzmann-distributed. The molecule is then subjected at $t > 0$ to time-varying external potential that couples directly to the mobile charge in the mixed-valence molecule. In the present work, the driver molecule is not explicitly modeled and it is assumed that its electronic state is controlled externally. Thus, we can neglect the electronic feedback between the driver and the driven molecules. The external potential fundamentally changes the shape of the intramolecular potential energy. For both the abrupt and non-abrupt drivers shown in Figure 2(b), the right metal center is favored at $t = \infty$. At $t = \infty$, the electronic and nuclear degrees-of-freedom of the mixed-valence molecule will once again be in thermal equilibrium, but with the electron localized on the right metal center. The challenge is to model and understand the kinetics of this nonequilibrium, driven ET process.

Our strategy for modeling the dynamics of ET in mixed-valence molecules begins by mapping the electronic degrees-of-freedom to a two-state model, where each state represents the electron localized on one of the metal centers. The electronic system is then coupled to one key intramolecular vibrational mode that is assumed to promote inner-sphere ET. For example, in the molecule that will serve as our prototype, diferrocenylacetylene (DFA, Figure 3), the most important vibrational mode is a collective asymmetric breathing motion of the pair of ferrocenyl groups. The vibrations of bridging groups have also been identified as important to ET in mixed-valence molecules.[21] The inner-sphere vibrational mode is coupled to a thermal bath, which represents all other degrees-of-freedom, including the other intramolecular vibrational modes. The thermal bath is, thus, indirectly connected to the electronic system via the vibrational mode. The thermal environment is modeled using the Lindblad formalism. Finally, the electronic degree-of-freedom is directly coupled to a time-dependent driving-potential. The resulting Hamiltonian can be solved fully quantum mechanically for various forms of the driving potential. We can extract a driven ET rate from the non-equilibrium (transient) dynamics of this system. Using a fully quantum mechanical approach in this initial study also provides useful benchmarks for future work using mixed quantum classical approaches that are applicable to larger systems.[22–29]

As a concrete example, we apply this model to the DFA molecule. DFA is typical of the type of molecule that could function in molecular QCA cells. We begin by calculating the intrinsic, thermally driven ET kinetics as a baseline. We observe that treating the inner-sphere vibration quantum mechanically is important. The model is then used to calculate a nonequilibrium field-driven ET rate, which allows us to explore the relationship between molecular parameters, like the reorganization energy and electronic coupling, and the switching rate of the external driver, which ultimately determines the operating speed in QCA devices. Once again, we find that a fully quantum mechanical

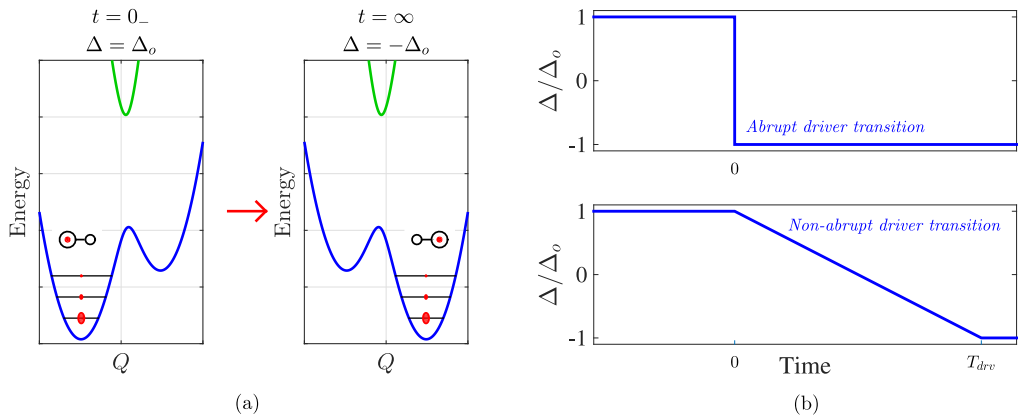

FIG. 2. The non-equilibrium ET process we consider here is driven by a time-varying external field. (a) The applied field results in a time-varying bias $\Delta(t)$ that initially localizes the electron on the left metal center. As $\Delta(t)$ changes, the adiabatic potential energy of the system (blue and green curves) changes, favoring localization upon the right metal center at $t = \infty$. (b) The driving potential $\Delta(t)$ may be either abrupt or non-abrupt, with driver transition duration T_{drv}. (a) Non-equilibrium field-driven ET. (b) External driving potential.

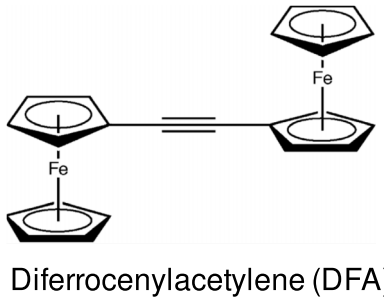

FIG. 3. Chemical structure of the mixed-valence diferrocenylacetylene (DFA) molecule. The two linked ferrocenyl groups provide a pair of charge localization sites separated by $a = 6.8$ Å.

treatment is necessary to capture tunneling and energy dissipation.

II. MODEL

The physical systems of interest are mixed-valence molecules with two charge localization centers, such as DFA (Figure 3), which has been synthesized, measured, and studied[30] for possible application in QCA. It is comprised of an electronic subsystem coupled to nuclear vibrational modes within the molecule. The electronic subsystem comprises of the information-bearing part of the QCA system, and the vibrational subsystem couples to the thermal environment, allowing excess energy from the electronic system to dissipate to the substrate. In addition, the electronic system is coupled to an external, time-dependent field. Figure 4 schematically represents this physical system and shows the coupling between each of the subsystems.

In the fully quantum treatment of this system, a two-state system is used to model the electronic subsystem, and a quantum harmonic oscillator is used to model the vibrational system. The electronic and vibrational subsystems are bilinearly coupled. Instead of explicitly modeling the degrees-of-freedom of the environment, we include the environmental effects phenomenologically through the Lindblad equation. The following discussion explains the modeling of each subsystem and their coupling.

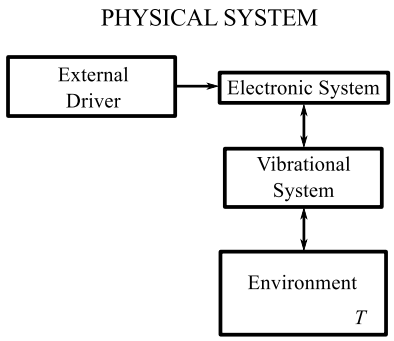

FIG. 4. Overview of the physical system of interest. A two-level electronic system is indirectly coupled to the environment via nuclear vibrational degrees-of-freedom. The electronic system is also coupled to a time-dependent external driver.

A. Electronic subsystem

The electronic subsystem is modeled as a mobile electron tunneling between two metal sites (or "dots") in a mixed valence molecule separated by a distance a. This is shown in Figure 5. The sites are labeled 0 and 1 and are also designated left and right (L and R, respectively). The two fully localized electronic states shown here are denoted $|0\rangle$ and $|1\rangle$, having polarizations $P = -1$ and $P = +1$, respectively. These states are assumed to be energetically degenerate and they provide a complete diabatic basis, $\{|0\rangle, |1\rangle\}$, for the electronic subsystem. Intramolecular ET enables device switching in QCA. A two-center, mixed-valence molecule functions as a two-dot QCA cell, so the terms "cell" and "molecule" are used interchangeably.

It is helpful to introduce the Pauli operators

$$\begin{aligned} \hat{\sigma}_x &= \hat{a}_L^\dagger \hat{a}_R + \hat{a}_L \hat{a}_R^\dagger, \\ \hat{\sigma}_y &= i\left(\hat{a}_L^\dagger \hat{a}_R - \hat{a}_L \hat{a}_R^\dagger\right), \text{ and} \\ \hat{\sigma}_z &= -\hat{a}_L^\dagger \hat{a}_L + \hat{a}_R^\dagger \hat{a}_R, \end{aligned} \tag{1}$$

where $\hat{a}_{L(R)}^\dagger$ and $\hat{a}_{L(R)}$ are the electron creation and annihilation operators on the left (right) dot. The Hamiltonian operator $\hat{H}_e$ for the electronic system, then, is

$$\hat{H}_e = -\gamma \hat{\sigma}_x + \frac{\Delta}{2}\hat{\sigma}_z. \tag{2}$$

Here, γ is the electronic coupling, which is often denoted as H_{AB} in the quantum chemistry literature, and can be obtained from calculations or experiment.

The bias Δ is the energy difference between the electron completely localized in diabatic states $|1\rangle$ and $|0\rangle$,

$$\Delta = \langle 1|\hat{H}_e|1\rangle - \langle 0|\hat{H}_e|0\rangle. \tag{3}$$

In the absence of an external field, the bias is zero because the two electronic states are degenerate by the symmetry of the DFA molecule. Other mixed-valence molecules, for example, with different metal centers or different ligands on the left and right sides of the molecule, would have a non-zero intramolecular bias Δ. An externally applied field or the field produced by neighboring molecules could also introduce a non-zero bias. For a driven ET process, $\Delta(t)$ is a time-varying function.

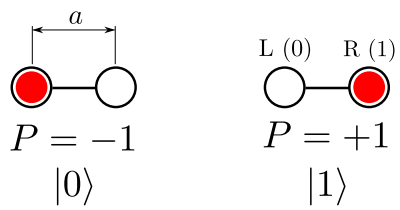

FIG. 5. Schematic representation of the electronic subsystem in the context of molecular QCA. Each metal site or "dot" is represented by a black circle, and a black line connects the pair, indicating a tunneling path and identifying the two dots as one molecule. One mobile electron is represented as a red disc. Dots are labeled "L" (left) and "R" (right), and numbered 0 and 1, respectively, with an inter-dot distance a. By symmetry, the electronic states are assumed to be degenerate in energy, and they have polarizations $P = \pm 1$. The two states provide a complete quantum mechanical basis, $\{|0\rangle, |1\rangle\}$, for the electronic subsystem.

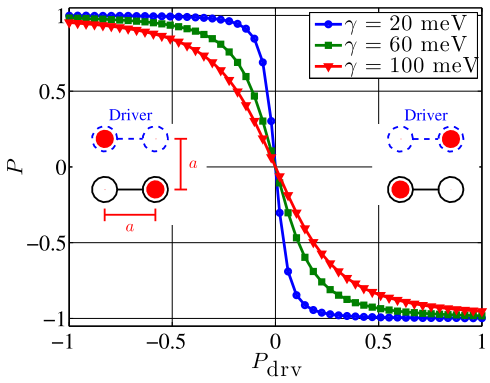

FIG. 6. Cell-cell response function for the molecular double-dot cell. The charge state of the driver cell biases the electronic state of the target cell, and Coulomb repulsion drives an ET event that represents a bit inversion. For this calculation, the inter-dot spacing of DFA molecule was used, $a = 6.8$ Å.

Information is encoded in the electronic system's polarization P, defined as the expectation value of $\hat{\sigma}_z$,

$$P \equiv \langle \hat{\sigma}_z \rangle = \mathrm{Tr}\ (\hat{\sigma}_z \hat{\rho}_e), \tag{4}$$

where $\hat{\rho}_e$ is the density operator for the electronic system. The polarization may vary continuously over the interval $(-1, 1)$ when the electron is not fully confined to either $|0\rangle$ or $|1\rangle$. The sign of P encodes a classical bit: "−" maps to the "0" bit and "+" maps to "1."

The response P of the electronic subsystem to an input driving polarization P_{drv} is shown in Figure 6. Here, a target cell has one neighbor cell, designated the "driver" cell, set at a distance a equal to the inter-dot distance. Thus, the dots of the driver and target cells form a square. The P_{drv} value determines the bias Δ for the target cell, and the output P is determined by the ground state of the target's electronic system. $|P_{\mathrm{drv}}|$ quantifies the input signal strength, and $|P|$ quantifies the output signal strength. For Figure 6, we used the inter-dot separation $a = 6.8$ Å, characteristic of the DFA molecule. This results in Δ varying over $[-623, 623]$ meV. While this implies that driving fields due to DFA molecules are ∼1 V/nm, field strengths of this magnitude are reasonable, given fields recently reported for biochemical molecular systems (∼10 V/nm).[31] The values of γ in Figure 6 were chosen to be typical of electronic couplings in mixed-valence molecules. Note that DFA has an electronic coupling of $\gamma = 50$ meV.

Figure 6 highlights two important behaviors in QCA. First, a bit inversion occurs between the driver and the target cell—the sign of the output polarization is opposite of the sign of the input polarization. Secondly, the response is nonlinear: a small input polarization induces a larger output polarization. The magnitude of the slope of this response curve at the origin, which can be considered a signal gain, increases when $\gamma/|\Delta|$ decreases. Large γ tends to delocalize the electron, while a large $|\Delta|$ enhances localization.

B. Vibrational subsystem and thermal environment

The vibrational component of the physical system is comprised of the nuclear displacements associated with the inner-sphere ET between the dots. Employing the Piepho, Krausz, and Schatz (PKS) model[32,33] for the isolated electron-vibrational system, we consider only the antisymmetric breathing mode displacement Q, which is closely coupled to ET.

The Hamiltonian $\hat{H}_v$ for the vibrational subsystem is a one dimensional harmonic oscillator,

$$\hat{H}_v = \frac{1}{2m}\hat{P}_Q^2 + \frac{m\omega^2}{2}\hat{Q}^2 = \hbar\omega\left(\hat{a}_Q^\dagger \hat{a}_Q + \frac{1}{2}\right). \tag{5}$$

The effective mass m and the frequency ω of the vibration may be obtained from quantum chemistry calculations, and $\hat{P}_Q$ and $\hat{Q}$ are the vibrational momentum and position operators. The first term in (5) corresponds to the kinetic energy of the oscillator and the second term to the potential energy. Note that these degrees-of-freedom represent an actual vibrational mode of the molecule and they are not representing a collective coordinate of the solvent. In other words, we are assuming that the electron transfer process is entirely governed by the external electric field and inner-sphere (i.e., intramolecular vibrational) processes. The environment does not electronically polarize the system. This is reasonable because in molecular QCA applications these molecules are isolated on surfaces in the absence of a polar solvent. $\hat{Q}$ and $\hat{P}_Q$ may be written in terms of the creation and annihilation operators $\hat{a}_Q^\dagger$ and $\hat{a}_Q$,

$$\begin{aligned} \hat{Q} &= \sqrt{\frac{\hbar}{2m\omega}}\left(\hat{a}_Q^\dagger + \hat{a}_Q\right), \\ \hat{P}_Q &= i\sqrt{\frac{m\omega\hbar}{2}}\left(\hat{a}_Q^\dagger - \hat{a}_Q\right). \end{aligned} \tag{6}$$

The quantum-mechanical Liouville equation describes dynamics of the isolated vibrational system,

$$\frac{d}{dt}\hat{\rho}_v = -\frac{i}{\hbar}\left[\hat{H}_v, \hat{\rho}_v\right], \tag{7}$$

where $[\hat{A}, \hat{B}]$ is the commutator of operators $\hat{A}$ and $\hat{B}$, and $\hat{\rho}_v$ is the density operator for the vibrational mode. The quantum Liouville equation is equivalent to the time-dependent Schrödinger equation, so the evolution described here is unitary, coherent, and reversible.[34,35]

To model the environmental effects on the vibration, we assume that the environment is Markovian and use the phenomenological Lindblad equation,[36,37]

$$\frac{d}{dt}\hat{\rho}_v = -\frac{i}{\hbar}\left[\hat{H}_v, \hat{\rho}_v\right] + \sum_{j=1}^{s}\hat{L}_j\hat{\rho}_v\hat{L}_j^\dagger - \frac{1}{2}\left\{\hat{L}_j^\dagger\hat{L}_j, \hat{\rho}_v\right\}. \tag{8}$$

The first term of (8) describes unitary evolution, and the summation in (8) describes the non-unitary and irreversible time evolution, including decoherence and dissipation. Here, $\{\hat{A}, \hat{B}\}$ is the anticommutator of operators $\hat{A}$ and $\hat{B}$, and $\hat{L}_j$ are Lindblad operators.[35]

We model the vibration-environment interaction using the two Lindblad operators,

$$\hat{L}_1 = \sqrt{\frac{1}{T_1}}\hat{a}_Q, \tag{9}$$

$$\hat{L}_2 = \exp\left(-\frac{\hbar\omega}{2k_BT}\right)\sqrt{\frac{1}{T_1}}\hat{a}_Q^\dagger, \tag{10}$$

where T is the temperature of the environment, k_B is the Boltzmann constant, and T_1 is the vibrational energy relaxation time. The rationale for utilizing the Lindblad equation is only to provide energy dissipation from the vibrational coordinate to the environment. It is not meant to mimic the polarization properties of a solvent. It is important to appreciate that the Lindblad model is phenomenological and that a more thorough description of energy dissipation would require a more sophisticated approach. However, the Lindblad model does contain the essential physics of exponential energy dissipation to the environment and it is appropriate here as we seek to gain the first understating of electric-field-driven electron transfer in mixed-valence molecules.

C. Combined vibronic system

The Holstein molecular-crystal model is used to treat the combined electron/vibration (vibronic) system in isolation.[38,39] The Hamiltonian that couples the electronic and vibrational subsystems, $\hat{H}_{ev}$, is

$$\hat{H}_{ev} = \frac{g_{ev}}{2}\hat{\sigma}_z\hat{Q}. \tag{11}$$

The vibronic coupling coefficient, g_{ev}, is related to the Marcus reorganization energy λ via

$$g_{ev} = \sqrt{2m\omega^2\lambda}. \tag{12}$$

The reorganization energy can be determined from quantum chemistry calculations or from spectroscopic measurements. It is important to note that we are implicitly assuming that the reorganization energy and the electronic and vibronic couplings are all unaffected by the imposed electric fields. In reality, sufficiently strong fields can have an effect on the reorganization energy and the electronic and vibronic coupling.[40] Understanding the effects of typical fields in molecular QCA applications will require future study and is an important design consideration.

D. Driven vibronic system

The Hamiltonian $\hat{H}(t)$ for the driven dynamical system without coupling to the environment is given by the sum of the electronic Hamiltonian $\hat{H}_e(t)$, the vibrational Hamiltonian $\hat{H}_v$, and the coupling $\hat{H}_{ev}$,[38,39,41]

$$\hat{H}(t) = -\gamma\hat{\sigma}_x + \frac{\Delta(t)}{2}\hat{\sigma}_z + \frac{g_{ev}}{2}\hat{\sigma}_z\hat{Q} + \frac{\hat{P}_Q^2}{2m} + \frac{m\omega^2\hat{Q}^2}{2}. \tag{13}$$

Note that the time-dependence enters the Hamiltonian purely through the bias potential, $\Delta(t)$. The assumption is that an external influence changes the relative energies of localizing

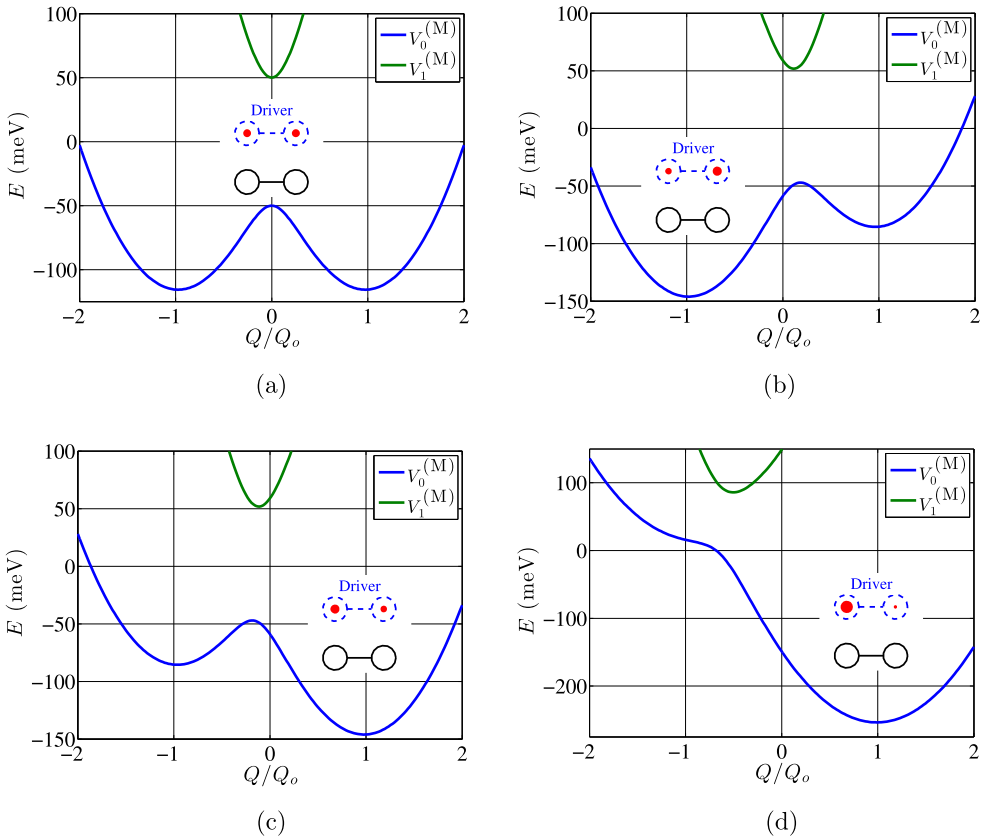

FIG. 7. Adiabatic potential energy curves for a symmetric mixed-valence molecule subject to different static external drivers as a function of the assumed classical vibrational coordinate, Q. The ground state $V_0^{(M)}(Q)$ is shown in blue, and the excited state $V_1^{(M)}(Q)$ is shown in green. (a) Unbiased case ($P_{drv} = 0$). (b) A slight bias leftward ($P_{drv} > 0$). (c) A slight bias rightward ($P_{drv} < 0$). (d) Strong rightward bias. Parameters appropriate to the DFA molecule were used for these calculations: $a = 6.8$ Å, $\gamma = 50$ meV, $\lambda = 440$ meV, $m = 5.6$ amu, and $f = \omega/2\pi = 298$ cm^{-1}. (a) Unbiased cell ($P_{drv} = 0$, $\Delta = 0$). (b) Slightly biased cell (leftward, $P_{drv} = 0.1$, $\Delta = 62.3$ meV). (c) Slightly biased cell (rightward, $P_{drv} = -0.1$, $\Delta = -62.3$ meV). (d) Strongly biased cell (rightward, $P_{drv} = -0.45$, $\Delta = -280$ meV).

the electron on the left and right sides of the mixed-valance molecule.

The dynamics of this system coupled to the thermal environment are described by the Lindblad equation,

$$\frac{d}{dt}\hat{\rho} = -\frac{i}{\hbar}\left[\hat{H},\hat{\rho}\right] + \sum_{j=1}^{s}\hat{L}_j\hat{\rho}\hat{L}_j^{\dagger} - \frac{1}{2}\left\{\hat{L}_j^{\dagger}\hat{L}_j,\hat{\rho}\right\}. \quad (14)$$

Here, $\hat{\rho}$ is the full density matrix for the driven vibronic system, and the operators $\hat{L}_j$ act only on the vibrational subsystem. Our description of driven ET in mixed-valence systems is based on the numerical solutions of Equation (14) with the time-dependent Hamiltonian in (13).

Any parameter of interest for the full system may be obtained from $\hat{\rho}$. For example, the energy of the system $\langle E\rangle$ is the expectation value of the Hamiltonian,

$$\langle E\rangle \equiv \langle\hat{H}\rangle = \mathrm{Tr}\left(\hat{H}\hat{\rho}\right). \quad (15)$$

Electronic (or vibrational) parameters may be obtained from a reduced density matrix $\hat{\rho}_e$ ($\hat{\rho}_v$) for the electron (vibration). The reduced density matrix $\hat{\rho}_e$ ($\hat{\rho}_v$) is found by tracing $\hat{\rho}$ over the degrees of freedom of the vibration (electron),

$$\begin{aligned}\hat{\rho}_e &= \mathrm{Tr}_v\hat{\rho} \text{ and}\\ \hat{\rho}_v &= \mathrm{Tr}_e\hat{\rho}.\end{aligned} \quad (16)$$

Here, $\mathrm{Tr}_{v(e)}$ denotes the partial trace over the degrees of freedom of the vibration (electron). Electronic polarization is obtained by applying (4) to $\hat{\rho}_e$. Additionally, it is helpful to calculate the probability $P_{L(R)}$ of finding the electron on the left (right) dot,

$$\begin{aligned}P_L &= \mathrm{Tr}\left(|0\rangle\langle 0|\hat{\rho}_e\right), \text{ and}\\ P_R &= \mathrm{Tr}\left(|1\rangle\langle 1|\hat{\rho}_e\right).\end{aligned} \quad (17)$$

Finally, the expectation value $\langle Q\rangle$ of the vibrational system is the expectation value of the position operator,

$$\langle Q\rangle \equiv \langle\hat{Q}\rangle = \mathrm{Tr}\left(\hat{Q}\hat{\rho}_v\right). \quad (18)$$

E. Connection to the Marcus model

The Marcus model for thermally driven ET is recovered by removing the external driver (i.e., by regarding the bias in Eq. (13), Δ, as a constant independent of time), and treating the vibrational coordinate, Q, classically ($\hat{Q} \longrightarrow Q$).[17] The reduced Hamiltonian, $\hat{H}^{(\mathrm{M})}(Q)$, that acts only on the electronic subsystem is

$$\hat{H}^{(\mathrm{M})}(Q) = -\gamma\hat{\sigma}_x + \frac{\Delta}{2}\hat{\sigma}_z + \frac{g_{ev}}{2}Q\hat{\sigma}_z + \frac{m\omega^2}{2}Q^2 \quad (19)$$

in the diabatic representation. The eigenvalues $V_k^{(\mathrm{M})}(Q)$ of (19) as functions of Q are the Marcus potential energy curves in the adiabatic representation,

$$\hat{H}^{(\mathrm{M})}(Q)\,|\Psi_k^e\rangle = V_k^{(\mathrm{M})}(Q)\,|\Psi_k^e\rangle, \quad (20)$$

where $|\Psi_k^e\rangle$ are the adiabatic electronic wave functions.

Figure 7 shows plots of the eigenvalues $V_0^{(\mathrm{M})}(Q)$ and $V_1^{(\mathrm{M})}(Q)$ using parameters in Eq. (19) appropriate for the DFA molecule. The horizontal axis is scaled to the equilibrium displacement Q_0 of the nuclear coordinate with the electron fully localized on one of the metal centers, given by

$$Q_0 = \frac{g_{ev}}{2m\omega^2}. \quad (21)$$

Figure 7(a) shows $V_0^{(\mathrm{M})}(Q)$ for no bias, $\Delta = 0$. This would be the scenario for an isolated DFA molecule. Here, the ground state Marcus potential is a symmetric double-well. A slight bias leftward ($P_{\mathrm{drv}} > 0$) or rightward ($P_{\mathrm{drv}} < 0$) favors one of the wells (Figures 7(b) and 7(c)). A strong bias eliminates the barrier and makes $V_0^{(\mathrm{M})}(Q)$ monostable (7(d)).

Is a quantum mechanical treatment of the vibrational coordinate necessary to describe field-driven ET in the DFA mixed-valence molecule? A calculation of the energy levels, E_n, of the fully quantum mechanical Hamiltonian in Eq. (13) with a time-independent bias is physically revealing. Figure 8 shows the ground-state adiabatic potential energy surface, $V_0^{(\mathrm{M})}(Q)$, with the energy levels superimposed for

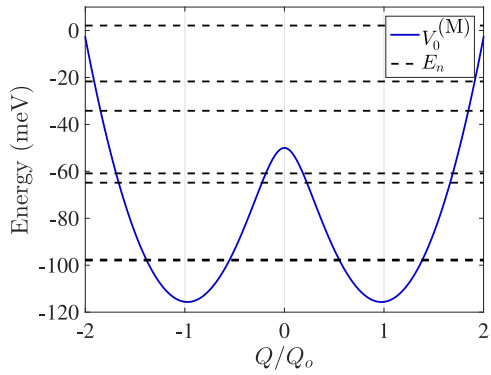

(a)

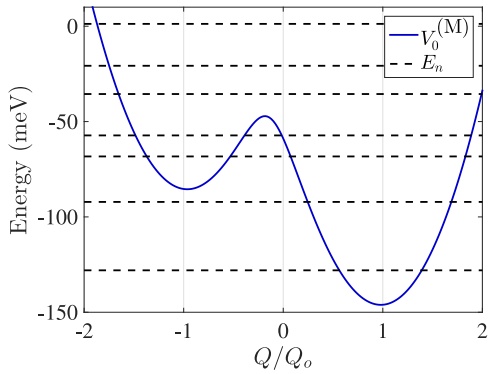

(b)

FIG. 8. Energy levels for the fully quantum mechanical system (a) under zero bias and (b) under a slight rightward bias. The blue curve is the adiabatic ground-state Marcus potential energy curve, $V_0^{(\mathrm{M})}(Q)$, where the vibrational degree-of-freedom is classical and the horizontal lines mark the eigenenergies, E_n, of a fully quantum mechanical treatment of the vibronic system. Parameters based on the DFA molecule were used here: $a = 6.8$ Å, $\gamma = 50$ meV, $\lambda = 440$ meV, $m = 5.6$ amu, and $f = \omega/2\pi = 298$ cm^{-1}. (a) Unbiased cell ($P_{\mathrm{drv}} = 0$, $\Delta = 0$). (b) Slightly biased cell (rightward, $P_{\mathrm{drv}} = -0.1$, $\Delta = -62.3$ meV).

two cases, zero bias (top panel) and a modest rightward bias (lower panel). In both cases, the energy level spacing is significant compared to the barrier height, which motivates our decision to treat the entire vibronic system quantum mechanically.

III. RESULTS

A. Calculations of the electron transfer rate driven by an abrupt change in bias

Here, we calculate a driven ET rate k by numerically solving Eq. (14) for the Hamiltonian in Eq. (13) for an abrupt change in bias (upper panel of Figure 2(b)). The calculations employed a fourth-order Runge-Kutta Dormand-Prince method as implemented in MATLAB.[42] This algorithm employs an adaptive time step. Note that we are treating the entire system quantum mechanically.

To set the initial state of the system we first apply a strong bias $\Delta(t<0)=\Delta_{\text{large}}$ to localize the electron on the left site. The system with this bias is described by a Hamiltonian $\hat{H}_{t<0}$. From that we can calculate the electron-vibration thermal density matrix $\hat{\rho}^{\text{th}}$,

$$\hat{\rho}^{\text{th}}=\frac{1}{Z}\exp\left(-\frac{\hat{H}_{t<0}}{k_BT}\right), \tag{22}$$

where Z is the partition function,

$$Z=\text{Tr}\left\{\exp\left(-\frac{\hat{H}_{t<0}}{k_BT}\right)\right\}. \tag{23}$$

The time evolution of the system coupled to the environment, with the bias fixed at Δ_{large}, is then calculated using Eq. (14) and the initial condition $\hat{\rho}_0(0)=\hat{\rho}^{\text{th}}$. This proceeds until the system no longer changes.

The switching of the system begins at $t=0$, when the driver is abruptly changed, abruptly altering the bias: $\Delta(t\geq 0)=\Delta_o$. This defines a new Hamiltonian $\hat{H}_{t\geq 0}$, which is constant over the interval $[0,\infty]$. Now, $\hat{\rho}(0)$, $\hat{H}_{t\geq 0}$, $\hat{L}_1$, and $\hat{L}_2$ are inputs to the Lindblad equation of Eq. (14). We solve Eq. (14) and extract the time it takes for the electron to transfer to the right dot and for the vibration to re-establish thermal equilibrium with the environment. This time is defined as t_{ET}, and the ET rate is its inverse: $k=t_{\text{ET}}^{-1}$.

We define an electron transfer time t_{ET} for the quantum system as the time when the probability $P_L(t)$ drops to a threshold value $P_L^{(\text{th})}$, here chosen to be 0.02. This choice is meant to physically capture the entire electron transfer process including the re-equilibration of the vibrational degrees-of-freedom to the new bias. A different choice of the threshold will slightly affect the numerical results, but not the qualitative behavior of the driven electron transfer process nor the physical understanding that is extracted from the results. Because of the driver, the direction of the electron transfer process is predetermined. Thus, the concepts of forward and backward electron transfer that are relevant in thermally driven electron transfer lose their meaning in the nonequilibrium, driven process.

1. The dependence of k on the vibration-environment coupling dissipation strength

After the abrupt change in the bias $\Delta(t)$, the vibration-environment coupling enables the system to re-equilibrate at a new electronic configuration. One might expect that increasing the environmental interaction would lead to shorter switching times. The results plotted in Figure 9 show this to be true for weak vibration-environment coupling but also show longer switching times in the high-coupling regime. Here, the target cell's polarization $P(t)$ is plotted as a function of time, scaled in units of the oscillation period $\tau_{\text{vib}}=2\pi/\omega$ of the vibrational system. The dimensionless ratio τ_{vib}/T_1 quantifies the strength of the vibration-environment coupling. For a weakly coupled environment, T_1 is large compared to the period of the vibration, resulting in low τ_{vib}/T_1. A strongly coupled environment has a low T_1 and a high τ_{vib}/T_1 ratio.

The behavior of $P(t)$ seen in Figure 9 can be understood in terms of damping on an oscillator. For low τ_{vib}/T_1, the vibration is an under-damped system, so that increasing environmental coupling shortens its response time, allowing a faster transfer of the electron. Eventually, a critical damping is reached, and further increases in the environmental coupling over-damp the system, causing longer switching times.

Figure 10 shows the dynamics of both the electronic and vibrational subsystems after an abrupt change in bias $\Delta(t)$ for the $\tau_{\text{vib}}/T_1=1$ case from Figure 9. The polarization $P(t)$ is shown in the upper plot, and the probability distribution for the vibrational system is shown in the coordinate Q and time t as a color map below. Here, red indicates high probability, and the white line is the expectation value of the vibrational coordinate in time $\langle Q(t)\rangle$. The two subsystems demonstrate two different responses: the electronic system has a smooth switch in $P(t)$, while the vibrational system has a highly delocalized and oscillatory probability distribution whose average, $\langle Q(t)\rangle$, is a damped oscillatory response. The electronic system is able to dissipate its energy before the vibration is done oscillating.

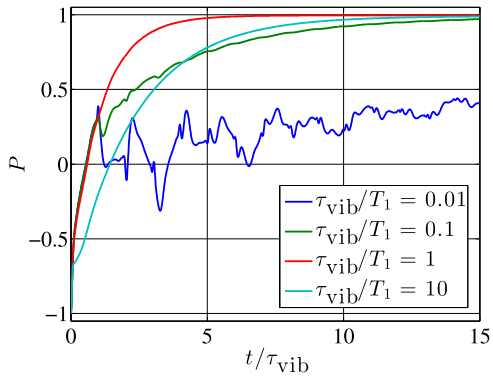

FIG. 9. Time evolution of polarization following an abrupt change in bias for various values of the vibrational lifetime T_1. For small values of the vibrational population lifetime compared to the period of the vibration ($\tau_{\text{vib}}/T_1=0.01, 0.1$, and 1.0), the switching event is faster for stronger vibration-environment coupling. However, when the environmental coupling becomes strong enough, further increasing this coupling slows the electronic switching response (compare the traces for $\tau_{\text{vib}}/T_1=1$ and 10). These calculations were performed with a thermal environment at $T=300$ K and with parameters appropriate to the DFA molecule: $a=6.8$ Å, $\gamma=50$ meV, $\lambda=440$ meV, $m=5.6$ amu, $f=298$ cm^{-1}, and $\Delta_0=-623$ meV.

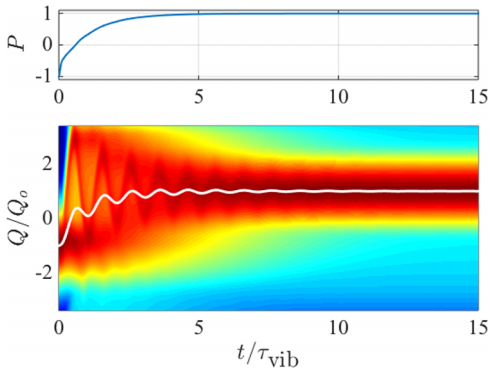

FIG. 10. Non-equilibrium response of the electronic polarization and the vibrational coordinate to an abrupt switch in bias $\Delta(t)$. The polarization response $P(t)$ is shown in the upper plot, and the color of the lower plot maps the probability distribution of the vibrational coordinate in space and time. A white line overlaying this distribution marks the expectation value, $\langle\hat{Q}(t)\rangle$, of the vibrational position in time. The electronic and vibrational responses—though coupled—are distinct. This calculation is the $\tau_{\text{vib}}/T_1 = 1$ case from Figure 9, with a thermal environment at $T = 300$ K and with parameters appropriate to the DFA molecule: $a = 6.8$ Å, $\gamma = 50$ meV, $\lambda = 440$ meV, $m = 5.6$ amu, $f = 298$ cm^{-1}, and $\Delta_0 = -623$ meV.

Figure 11 shows the dependence of the electron transfer rate, k, on the vibration-environment coupling strength, τ_{vib}/T_1, and is consistent with the above picture of damping upon the system. The peak in $k\,(\tau_{\text{vib}}/T_1)$ reflects critical damping, above which the system is over-damped, and below which the system is under-damped. The rate, $k\,(\tau_{\text{vib}}/T_1)$, is plotted both at zero temperature and at room temperature. The higher temperature broadens and slightly lowers the peak in $k\,(\tau_{\text{vib}}/T_1)$. Note that the non-zero rate of driven ET transfer at $T = 0$ differs dramatically from the behavior of a thermally driven ET process, where the rate is 0 at $T = 0$ in the absence of tunneling.[43]

2. The dependence of k on temperature

Figure 12 shows the temperature dependence of the ET rate k calculated in the fully quantum-mechanical treatment

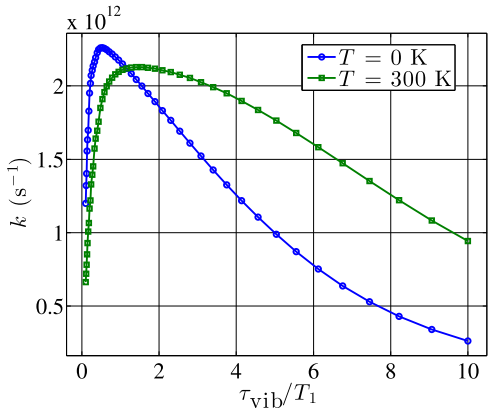

FIG. 11. Driven ET rate k as a function of environmental coupling, τ_{vib}/T_1, after an abrupt change in bias $\Delta(t)$. The electronic response exhibits the behavior of a damped system, with critical damping at the peak in $k\,(\tau_{\text{vib}}/T_1)$. Weaker coupling under-damps the system, and stronger coupling over-damps the system, slowing its response. These calculations were performed at $T = 0$ and $T = 300$ K, with parameters appropriate to the DFA molecule: $a = 6.8$ Å, $\gamma = 50$ meV, $\lambda = 440$ meV, $m = 5.6$ amu, $f = 298$ cm^{-1}, and $\Delta_0 = -623$ meV.

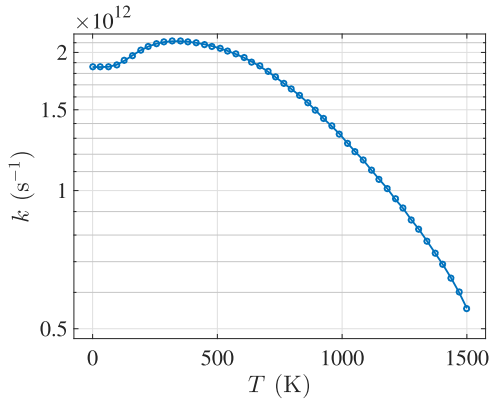

FIG. 12. ET rate, k, as a function of temperature, T, after an abrupt change in bias $\Delta(t)$. The driven ET rate $k\,(T)$ does not vary strongly with temperature; it varies by less than an order of magnitude over a very wide range of temperatures. These calculations were performed with parameters appropriate to the DFA molecule: $a = 6.8$ Å, $\gamma = 50$ meV, $\lambda = 440$ meV, $m = 5.6$ amu, $f = 298$ cm^{-1}, and $\Delta_o = -623$ meV. The vibration-environment coupling strength was set to $\tau_{\text{vib}}/T_1 = 2$.

following an abrupt change in Δ. In driven, non-equilibrium system, a $k\,(T)$ variation of less than one order of magnitude is seen over a large T range from 0 to 1500 K. The DFA molecule is one of the many systems exhibiting a largely temperature-independent ET rate.[44]

3. The dependence of k on bias Δ_0

Figure 13 shows the dependence of the electron transfer rate k on the final applied driving bias Δ_0 after the abrupt change in $\Delta\,(t)$. In the weakly driven case (small $|\Delta_o|$), increasing the magnitude of the driving bias leads to higher rates k, as might be expected. In the strongly driven case (high $|\Delta_o|$), there is considerably more electronic energy to dissipate via the vibrations, and longer switching times result. The rate constant in Figure 13 is bimodal with respect to Δ_0. In particular, k has a large peak at approximately 340 meV and a smaller peak at 540 meV, which are separated by a minimum

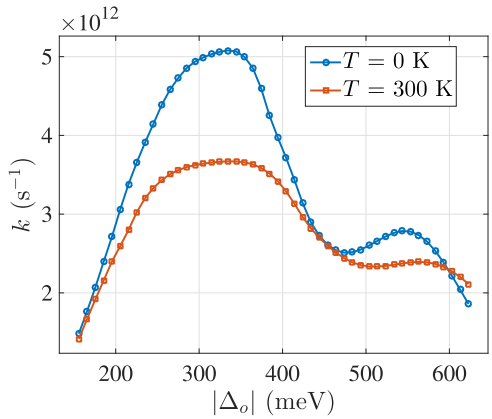

FIG. 13. The dependence of the ET rate k on driving bias Δ_0 after an abrupt change in bias. These calculations were performed with a thermal environment at $T = 0$ and $T = 300$ K with parameters appropriate to the DFA molecule: $a = 6.8$ Å, $\gamma = 50$ meV, $\lambda = 440$ meV, $m = 5.6$ amu, and $f = 298$ cm^{-1}. The vibration-environment coupling strength was set to $\tau_{\text{vib}}/T_1 = 2$.

at 440 meV. Interestingly, in the diabatic representation, 440 meV represents the transition into the Marcus inverted regime (i.e., where one quadratic diabatic potential energy curve intersects the other quadratic diabatic potential energy curve at its minimum).[14,45] One might then expect k to exhibit a maximum at 440 meV, but this neglects the abruptness of the driving bias and the electronic coupling, γ, of 50 meV. Immediately after the bias is abruptly changed to $\Delta_o = -440$ meV, the vibronic state of the system is exactly where the two diabatic curves cross, but this is also where the two adiabatic potentials are maximally separated. This results in a minimum value of k because of electronically nonadiabatic effects. In contrast, for $\Delta_o = -440$ meV $+2\gamma = -340$ meV, the vibronic state coincides with the barrierless ground adiabatic state and k has a maximum. At $\Delta_o = -440$ meV $-2\gamma = -540$ meV the vibronic state coincides with the excited adiabatic state and k exhibits a second maximum, albeit substantially smaller than the maximum at $\Delta_o = -340$ meV. As previously seen, this system has $k\left(|\Delta_0|\right)|_{T=0} \neq 0$, while a thermally driven ET process would have a rate of zero in the absence of tunneling.[43]

4. The dependence of k on the electronic coupling strength

Figure 14 shows the dependence of electron transfer rate k on the electronic coupling strength, γ, after an abrupt change in the bias. For low γ, an increase in the electronic coupling strength results in a higher ET rate at both 0 and 300 K because larger electronic coupling allows for faster transfer of charge. At higher γ, however, $k\,(\gamma)$ peaks and then declines. Here, the delocalizing effect from high γ becomes more significant and competes with the localizing effects of Δ and λ. Thus, when raising γ in the high-γ regime, an increasingly delocalized electron takes longer to coalesce on the right side of the molecule, resulting in a longer t_{ET} and thus a lower rate, k. This contrasts significantly from the behavior of thermally driven ET, where the ET rate increases monotonically with increasing γ. The rate in a thermally driven system is also zero for $\gamma = 0$, but in the driven-case the change in the topology of the ground adiabatic potential still allows for ET even with zero electronic coupling.

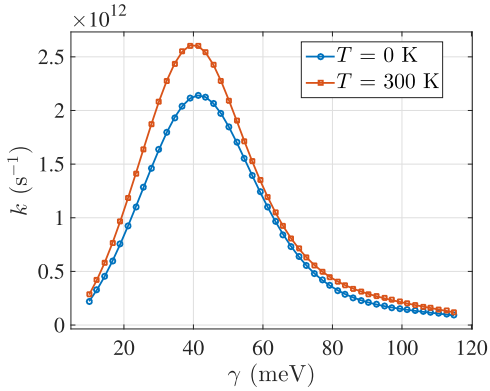

FIG. 14. The dependence of the ET rate k on the electronic coupling strength, γ, after an abrupt change in bias. At low γ, reducing electronic confinement (increasing γ) allows faster transfer of the electron, and thus higher k. At high γ, the electron is delocalized. Increasing γ exacerbates this, and the electron coalesces more slowly upon the right metal center of the mixed-valence molecule, thus reducing k. These calculations were performed with a thermal environment at $T = 0$ K and $T = 300$ K with parameters characteristic of the DFA molecule: $a = 6.8$ Å, $\Delta_0 = -623$ meV, $\lambda = 440$ meV, $m = 5.6$ amu, and $f = 298$ cm^{-1}. The vibration-environment coupling strength was set to $\tau_{\mathrm{vib}}/T_1 = 2$.

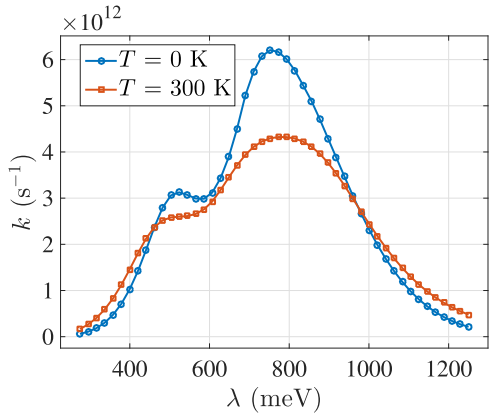

FIG. 15. ET rate k as a function of reorganization energy λ after an abrupt change in bias. These calculations were performed with a thermal environment at $T = 0$ K and $T = 300$ K with parameters characteristic of the DFA molecule: $a = 6.8$ Å, $\gamma = 50$ meV, $\Delta_0 = -623$ meV, $m = 5.6$ amu, and $f = 298$ cm^{-1}. The vibrational-environment coupling strength was set to $\tau_{\mathrm{vib}}/T_1 = 2$.

5. The dependence of k on reorganization energy

For an electron transfer driven by an abrupt change in bias, the dependence of the ET rate, k, on reorganization energy λ is shown in Figure 15. In the small-λ regime, weak vibronic coupling results in low vibronic power dissipation, impeding the overall electron-to-environment energy transfer. Thus, in the small-λ regime, increasing λ enables faster energy transfer resulting in reduced t_{ET} and increased $k\,(\lambda)$. In the high-λ regime, however, vibronic power dissipation no longer limits the speed of electronic switching. Here, the electron and vibration are so strongly coupled that they respond as a polaron, resulting in sluggish electronic switching. The

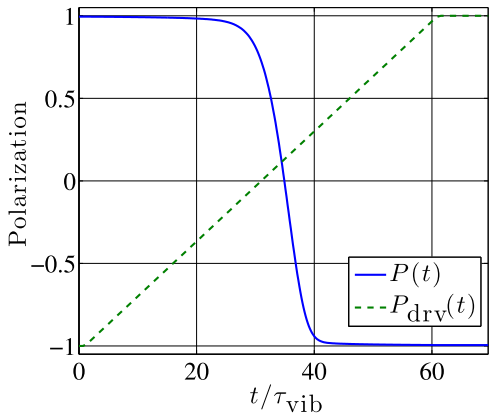

FIG. 16. A ramped driver induces an ET transfer in a mixed-valence molecule. The dashed green line shows the driver polarization starting at -1, with a ramped transition to $P_{\mathrm{drv}} = +1$ over a duration of $T_{\mathrm{drv}} = 60\tau_{\mathrm{vib}}$. This drives a non-linear electronic switch in $P(t)$ (blue trace). Here, parameters based on the DFA molecule were used: $a = 6.8$ Å, $\gamma = 50$ meV, $\lambda = 440$ meV, $m = 5.6$ amu, and $f = 298$ cm^{-1}. The vibrational-environment coupling strength is set to $\tau_{\mathrm{vib}}/T_1 = 2$, and the temperature is $T = 300$ K.

speed of the switching event is degraded further with stronger vibronic coupling. There is a close connection between the results in Figures 13 and 15. Physically, both results exhibit bimodal behavior for the same reasons. For a fixed change in bias, altering the reorganization energy effectively changes the relative shapes of the parabolic diabatic potential energy curves. At small reorganization energy, below approximately 580 meV, the system is in the Marcus inverted regime.[14,45] The large peak at approximately 750 meV corresponds to a case where the abrupt change in bias causes the vibronic state to exactly coincide with the ground adiabatic state. The smaller peak at approximately 500 meV is where the abrupt change in bias causes the vibronic state to exactly coincide with the excited adiabatic state.

B. Dynamics of electron transfer with a ramped driving potential

In this subsection we will consider the ET dynamics when the molecule is subjected to a ramped driving potential. In Figure (16), the mixed-valence molecule of interest starts at $t = 0$ in thermal equilibrium with its environment, and with the electron fully localized on the right side of the molecule. At $t = 1\tau_{\text{vib}}$, $P_{\text{drv}}(t)$ commences a ramped transition of duration $T_{\text{drv}} = 60\tau_{\text{vib}}$ from -1 to 1. Once the driver reaches $P_{\text{drv}}(t) = 1$ it remains constant in time, and the electron will complete its equilibration on the left side of the molecule. The dynamics of this process are calculated fully quantum-mechanically by numerically solving Eq. (14) with the Hamiltonian in Eq. (13) with the ramped bias potential.

Figure 17 shows the energetics of this switching event with a ramped driver, using the parameters of the DFA molecule. The panels of Figure 17 are sequential snapshots in time of the overall system's instantaneous energy expectation value $\langle E(t)\rangle$ and vibrational coordinate expectation value $\langle Q(t)\rangle$ marked using a red circle. The trajectory of the $(\langle Q(t)\rangle, \langle E(t)\rangle)$ coordinate is marked by a red line. The instantaneous ground adiabatic potential energy surface $V_0^{(\text{M})}(Q,t)$ is shown in a blue line, and its four lowest eigenvalues $E_n(t)$, $n \in \{0,1,2,3\}$ are marked using horizontal

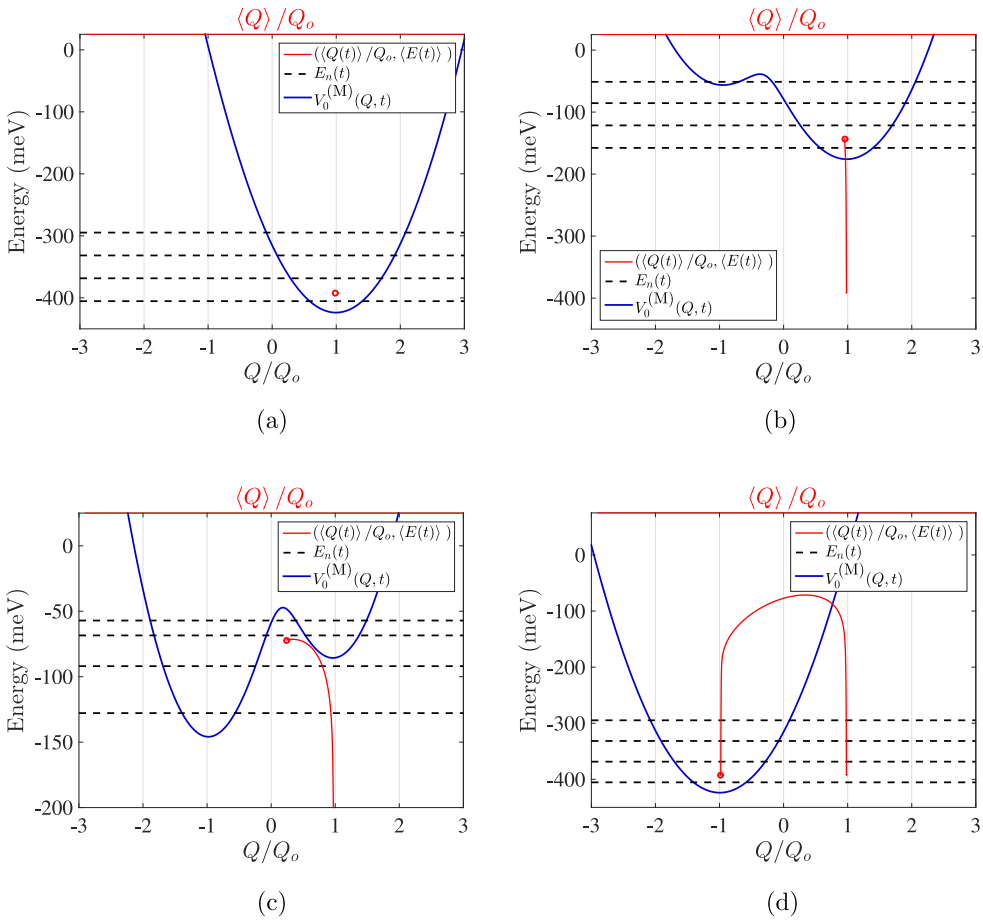

FIG. 17. Snapshots of a nonequilibrium ET event in a mixed-valence molecule driven by a ramped potential. In each plot, a red circle marks the instantaneous expectation value of energy $\langle E(t)\rangle$ and the expectation value of the vibrational coordinate $\langle Q(t)\rangle$ for the fully quantum mechanical system. A red line marks its trajectory. A blue line shows the instantaneous adiabatic ground-state potential, $V_0^{(\text{M})}(Q,t)$, and its four lowest energies, $E_n(t)$ ($n \in \{0,1,2,3\}$), are denoted using dashed black horizontal lines. This is the same evolution yielding the electronic polarization picture of Figure 16. (a) The system starts in equilibrium under a rightward bias from a fully polarized driver with $P_{\text{drv}}(t) = -1$ and in thermal equilibrium with the environment at 300 K. (b) At $t = 25\tau_{\text{vib}}$, the linear transition in $P_{\text{drv}}(t)$ has begun, and the system is excited, but $\langle Q(t)\rangle$ remains centered on the lowest of the bistable regions of the adiabatic potential energy surface. The bias remains rightward in Q (i.e., $\Delta(t) < 0$). (c) At $t = 34\tau_{\text{vib}}$, the system tunnels through the $V_0^{(\text{M})}(Q,t)$ barrier, driven by a leftward bias [$\Delta(t) > 0$]. (d) The switching event is complete by $t = 65\tau_{\text{vib}}$, and the electronic subsystem has transferred all of its energy to the thermal environment via the vibration. The vibrational coordinate has relaxed to its new equilibrium position above the bottom of the well in $V_0^{(\text{M})}(Q,t)$. (a) $t = 0$. (b) $t = 25\tau_{\text{vib}}$. (c) $t = 34\tau_{\text{vib}}$. (d) $t = 65\tau_{\text{vib}}$.

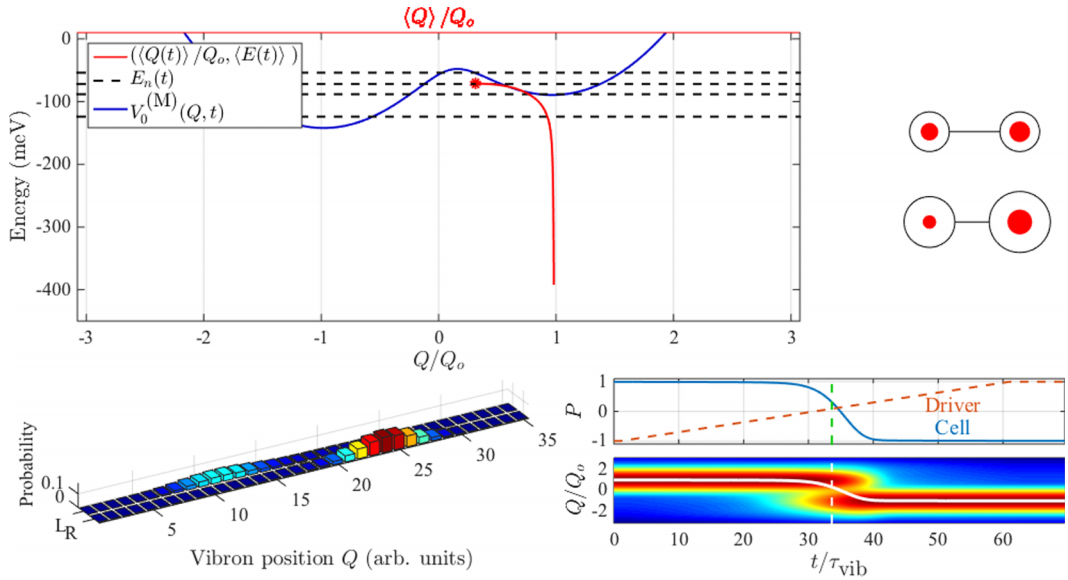

FIG. 18. Dynamics of field-driven electron transfer (ET) in a mixed-valence molecule. A neighbor molecule undergoes a ramped polarization switch, which drives ET in the target cell. *Upper left*: a coordinate $(\langle Q(t)\rangle, \langle E(t)\rangle)$ (red dot) marks the expectation values of energy $\langle E(t)\rangle$ and the vibrational coordinate $\langle Q(t)\rangle$ in time, and its trajectory is marked by a red line. The instantaneous adiabatic potential energy surface $V_0^{(M)}(Q,t)$ is plotted in blue, along with its four lowest eigenenergies, $E_n(t)$, $n \in \{0,1,2,3\}$, (dashed black lines). *Upper right*: a schematic depiction of the charge configuration of the driver cell (top) and target molecule (bottom). Black circles represent electron localization sites, and the radius of the red discs indicates the probability of finding a mobile electron on each dot. For the target cell, the dot radius also encodes the expectation value of vibrational coordinate: an enlarged R dot with a smaller L dot indicates $\langle Q(t)\rangle > 0$; and a smaller R dot with larger L dot indicates $\langle Q(t)\rangle < 0$. *Lower right*: the time dependence of driver and target cell polarizations (top plot); and vibrational coordinate probability distribution over Q and t (bottom plot). In the color map, red indicates high probability, and blue is for low probability. The expectation value of the coordinate $\langle Q(t)\rangle$ is plotted in white, and the time t is indicated using a vertical dashed line. *Lower left*: the instantaneous probability distribution of the system is plotted over electronic position (L or R) and Q for each of the eigenvalues of the vibrational position operator $\hat{Q}$. (Multimedia view) [URL: http://dx.doi.org/10.1063/1.4955113.1]

dashed black lines. The four plots of Figure 17 show the following.

1. **The initial condition (Figure 17(a))**. At $t = 0$, the system is in thermal equilibrium with the environment at $T = 300$ K, with $\langle Q(0)\rangle = Q_0$. Here, $\langle Q(0)\rangle$ coincides with the minimum in the adiabatic potential energy, $V_0^{(M)}(Q,t)$. The value of $\langle E(0)\rangle$ is above $E_0(t)$ because there is some population in the excited vibrational states at finite temperature.
2. **Excitation (Figure 17(b))**. At $t = 25\tau_{vib}$, the linear transition in $P_{drv}(t)$ is well underway, but $P_{drv}(t)$ has not yet changed sign, and the bias remains negative (thus, $+Q_0$ is favored); however, the driver has excited the system relative to the initial state. In the instantaneous adiabatic potential, a barrier has formed and the system now is bistable, with a minima at $Q = \pm Q_0$.
3. **Switching via quantum-mechanical tunneling (Figure 17(c))**. At $t = 34\tau_{vib}$, $P_{drv}(t)$ has switched sign so that the bias is now positive ($\Delta > 0$), and $-Q_0$ is preferred. The expectation value of the vibronic coordinate $\langle Q(t)\rangle$ has begun to displace leftward. The system now exhibits quantum mechanical tunneling, as the $(\langle Q(t)\rangle, \langle E(t)\rangle)$ point is moving *through* the barrier in $V_0^{(M)}(Q,t)$ along a classically forbidden trajectory.
4. **Relaxation (Figure 17(d))**. By $t = 61\tau_{vib}$, the transition in $P_{drv}(t)$ is complete, and by $t = 65\tau_{vib}$ the system has relaxed to a new equilibrium configuration: all the energy injected by the driver to the vibronic system is transferred to the thermal environment. The adiabatic potential energy, $V_0^{(M)}(Q,t)$, is once again monostable with its minimum at $Q = -Q_0$.

A video of the time evolution presented in Figures 16 and 17 also is available. Figure 18 (Multimedia view) provides a snapshot of the video, which shows dynamic plots of: the energetics shown in Figure 17; the instantaneous charge configuration of the driver and target cell, shown schematically; the time-varying target and driver polarization, along with the vibrational coordinate probability distribution over space and time; and the instantaneous vibronic probability distribution.

IV. CONCLUSIONS

We have modeled the nonequilibrium ET in a mixed-valence molecule driven by the electric field of a neighboring molecule. We include the direct coupling of the electronic degrees of freedom to the principal inner-sphere vibration —the antisymmetric breathing mode associated with ligand relaxation around the transferring charge. This vibrational motion is then coupled dissipatively to a thermal environment. We calculate the Coulombically driven nonequilibrium switching of the charge in time and calculate the driven ET transfer rate. This process is distinct from thermally driven ET processes but is very relevant for molecular electronics in the QCA paradigm. We have used the specific parameters of a DFA molecule which has been shown to be of interest in this regard.

Examination of the energy eigenstates shows that the fully quantum mechanical treatment of the ET motion is required.

Intermolecular fields result in a large change in the potential energy landscape of the molecule—beyond that which could be accounted for by perturbation theory. We considered both abrupt switching and a gradual ramping potential. The driven ET switching rate is only weakly temperature dependent and remains non-zero at zero temperature. Quantum effects are evident, as is the competition between the electronic coupling and the nuclear reorganization energy.

We have modeled only the primary vibrational motion coupled to the ET process; improvements to the current approach might be to include several vibrational modes. The phenomenological Lindblad treatment of environmental coupling, while adequate for our purposes here, could also be improved.

These results suggest that QCA cells implemented using DFA or similar molecules can operate at high speeds. Driven ET rates in the terahertz range were calculated for the DFA molecule, and through the design of other QCA candidate molecules, still higher rates may be possible. The interesting problem of optimal heat-sinking the molecular devices will need to be explored in the context of preserving signal integrity as well as power dissipation.

ACKNOWLEDGMENTS

The authors thank Yuhui Lu (Holy Cross College, Notre Dame, IN) for insightful discussion. This material is based upon work supported by the National Science Foundation (NSF) under Grant No. CHE-1124762 and Graduate Research Fellowship Grant No. DGE-1313583.

[1]J. Jiao, G. L. Long, F. Grandjean, A. M. Beatty, and T. P. Fehlner, J. Am. Chem. Soc. **125**, 7522 (2003).
[2]S. B. Braun-Sand and O. Wiest, J. Phys. Chem. A **107**, 285 (2003).
[3]S. B. Braun-Sand and O. Wiest, J. Phys. Chem. B **107**, 9624 (2003).
[4]Y. G. Zhao, D. Guo, Y. Liu, C. He, and C. Y. Duan, Chem. Commun. **2008**, 5725.
[5]V. N. Nemykin, G. T. Rohde, C. D. Barrett, R. G. Hadt, C. Bizzarri, P. Galloni, B. Floris, I. Nowik, R. H. Herber, A. G. Marrani, R. Zanoni, and N. M. Loim, J. Am. Chem. Soc. **131**, 14969 (2009).
[6]Y. Lu, R. Quardokus, C. S. Lent, F. Justaud, C. Lapinte, and S. A. Kandel, J. Am. Chem. Soc. **132**, 13519 (2010).
[7]Y. Lu and C. S. Lent, Chem. Phys. Lett. **582**, 86 (2013).
[8]B. Tsukerblat, A. Palii, J. M. Clemente-Juan, and E. Coronado, J. Chem. Phys. **143**, 134307 (2015).
[9]J. A. Christie, R. P. Forrest, S. A. Corcelli, N. A. Wasio, R. C. Quardokus, R. Brown, S. A. Kandel, Y. Lu, C. S. Lent, and K. W. Henderson, Angew. Chem., Int. Ed. **54**, 15448 (2015).
[10]P. D. Tougaw and C. S. Lent, J. Appl. Phys. **75**, 1818 (1994).
[11]C. S. Lent, Science **288**, 1597 (2000).
[12]C. S. Lent, B. Isaksen, and M. Lieberman, J. Am. Chem. Soc. **125**, 1056 (2003).
[13]J. C. Goeltz and C. P. Kubiak, J. Phys. Chem. C **112**, 8114 (2008).
[14]R. A. Marcus, Rev. Mod. Phys. **65**, 599 (1993).
[15]H. B. Gray and J. R. Winkler, Annu. Rev. Biochem. **65**, 537 (1996).
[16]P. F. Barbara, T. J. Meyer, and M. A. Ratner, J. Phys. Chem. **100**, 13148 (1996).
[17]R. A. Marcus, J. Chem. Phys. **24**, 966 (1956).
[18]N. H. Hush, Trans. Faraday Soc. **57**, 557 (1961).
[19]N. R. Kestner, J. Logan, and J. Jortner, J. Phys. Chem. **78**, 2148 (1974).
[20]J. Jortner, J. Chem. Phys. **64**, 4860 (1976).
[21]C. H. Londergan and C. P. Kubiak, J. Phys. Chem. A **107**, 9301 (2003).
[22]H.-T. Chen and D. R. Reichman, J. Chem. Phys. **114**, 094104 (2016).
[23]P. V. Parandekar and J. C. Tully, J. Chem. Phys. **122**, 094102 (2005).
[24]J. R. Schmidt, P. V. Parandekar, and J. C. Tully, J. Chem. Phys. **129**, 044104 (2008).
[25]G. A. Meek and B. G. Levine, J. Phys. Chem. Lett. **5**, 2351 (2014).
[26]M. C. Sherman and S. A. Corcelli, J. Chem. Phys. **142**, 024110 (2015).
[27]A. Jain and J. E. Subotnik, J. Chem. Phys. **143**, 134107 (2015).
[28]A. Jain, M. F. Herman, W. Ouyang, and J. E. Subotnik, J. Chem. Phys. **143**, 134106 (2015).
[29]A. Jain and J. E. Subotnik, J. Phys. Chem. Lett. **6**, 4809 (2015).
[30]R. C. Quardokus, N. A. Wasio, R. P. Forrest, C. S. Lent, S. A. Corcelli, J. A. Christie, K. W. Henderson, and S. A. Kandel, Phys. Chem. Chem. Phys. **15**, 6973 (2013).
[31]S. D. Fried, S. Bagchi, and S. G. Boxer, Science **346**, 1510 (2014).
[32]K. Y. Wong and P. N. Schatz, Prog. Inorg. Chem. **28**, 369 (1981).
[33]S. B. Piepho, E. R. Krausz, and P. N. Schatz, J. Am. Chem. Soc. **100**, 2996 (1978).
[34]M. A. Nielsen and I. L. Chuang, *Quantum Computing and Quantum Information* (Cambridge University Press, 2000).
[35]H.-P. Breuer and F. Petruccione, *The Theory of Open Quantum Systems* (Oxford Scholarship Online, 2010).
[36]V. Gorini, A. Kossakowski, and E. C. G. Sudarshan, J. Math. Phys. **17**, 821 (1976).
[37]G. Lindblad, Commun. Math. Phys. **48**, 119 (1967).
[38]T. Holstein, Ann. Phys. **8**, 325 (1959).
[39]K. V. Mikkelsen and M. A. Ratner, Chem. Rev. **87**, 113 (1987).
[40]P. Song, Y. Li, F. Ma, T. Pullerits, and M. Sun, J. Phys. Chem. C **117**, 15879 (2013).
[41]G. C. Schatz and M. A. Ratner, *Quantum Mechanics in Chemistry* (Dover Publications, Inc., 2002).
[42]J. R. Dormand and P. J. Prince, J. Comput. Appl. Math. **6**, 19 (1980).
[43]G. Lang, E. Palafino, and U. Weiss, Chem. Phys. **244**, 111 (1999).
[44]W. B. Davis, M. A. Ratner, and M. R. Wasielewski, J. Am. Chem. Soc. **123**, 7877 (2001).
[45]J. R. Miller, L. T. Calcaterra, and G. L. Closs, J. Am. Chem. Soc. **106**, 3047 (1984).